



Measurement of resistance curves in the longitudinal failure of composites using digital image correlation

G. Catalanotti^a, P.P. Camanho^{a,*}, J. Xavier^b, C.G. Dávila^c, A.T. Marques^a

^a DEMec, Faculdade de Engenharia, Universidade do Porto, Rua Dr. Roberto Frias, 4200-465 Porto, Portugal

^b CITAB/UTAD, Engenharias I, Apartado 1013 5001, 801 Vila Real, Portugal

^c NASA Langley Research Center, Hampton, VA, USA

ARTICLE INFO

Article history:

Received 7 April 2010

Received in revised form 16 July 2010

Accepted 22 July 2010

Available online 1 August 2010

Keywords:

A. Polymer–matrix composites (PMCs)

B. Fracture toughness

ABSTRACT

This paper presents a new methodology to measure the crack resistance curves associated with fiber-dominated failure modes in polymer–matrix composites. The crack resistance curves not only characterize the fracture toughness of the material, but are also the basis for the identification of the parameters of the softening laws used in the numerical simulation of fracture in composite materials. The proposed method is based on the identification of the crack tip location using Digital Image Correlation and the calculation of the J -integral directly from the test data using a simple expression derived for cross-ply composite laminates. It is shown that the results obtained using the proposed methodology yield crack resistance curves similar to those obtained using Finite Element based methods for compact tension carbon–epoxy specimens. However, it is also shown that, while the Digital Image Correlation based technique mitigates the problems resulting from Finite Element based data reduction schemes applied to compact compression tests, the delamination that accompanies the propagation of a kink-band renders compact compression test specimens unsuitable to measure resistance curves associated with fiber kinking.

© 2010 Elsevier Ltd. All rights reserved.

1. Introduction

Despite the significant advances in the analysis models for the prediction of fracture in composite materials such as advanced failure criteria and associated damage models [1–7], sophisticated kinematic representations of failure mechanisms [8,9], and cohesive elements to deal with delamination [10,11], the accurate prediction of intralaminar fracture mechanisms still presents several challenges.

The majority of existing models for intralaminar fracture of polymer-based composite materials reinforced by carbon-fibers are based on softening constitutive models [7]. The shape of the softening law is often assumed to be inconsequential for the prediction of fracture, provided that it is defined as a function of the fracture toughness. While this assumption is valid under small-scale bridging conditions, the shape of the cohesive law plays a fundamental role in the prediction of fracture under large-scale bridging conditions [12]. When crack propagation includes different energy dissipation mechanisms that act over different length scales, the nature of these mechanisms must be appropriately accounted in the cohesive law.

* Corresponding author. Tel.: +351 225081753; fax: +351 225081315.

E-mail address: pcamanho@fe.up.pt (P.P. Camanho).

Several failure mechanisms including fiber tensile fracture, fiber–matrix pull-out and matrix cracking are present when a crack propagates in a plane perpendicular to the fiber direction. To account for these different failure mechanisms, a combined linear–exponential softening law for fiber tensile fracture has been proposed [5,6], and it was demonstrated that a simple linear softening law is unable to predict the load–displacement relation obtained in a cross-ply Compact Tension (CT) test specimen, while a bi-linear softening law provides an accurate prediction [13]. The definition of the parameters used in the softening law related to the fiber-dominated failure mechanisms is based on the experimental determination of the crack resistance curve (R -curve) of the Compact Tension (CT) and Compact Compression (CC) test specimens proposed by Pinho [14]. However, these test specimens present some problems that are yet to be resolved.

Laffan et al. [15] performed a detailed investigation of the different data reduction methods available for the measurement of the ply fracture toughness associated with mode I fiber tensile failure and concluded that the data reduction methods based on Finite Elements (e.g. by using the J -integral [16]) eliminate errors that occur in the compliance calibration method, which result from the differentiation of a fitted curve. Based on a detailed comparison of the area method, the J -integral/Virtual Crack Closure Technique, the ASTM E399 [17] standard, the compliance calibration and the modified compliance calibration methods, the authors concluded

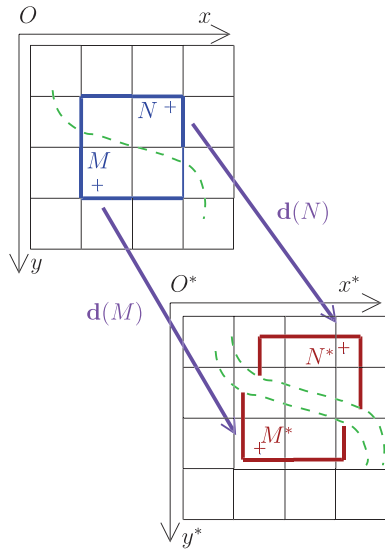


Fig. 1. Points M and N before and after crack propagation.

that the modified compliance calibration method using an effective crack length was the most appropriate data reduction scheme because it provides consistent results and it does not require an optically measured crack length [15].

The Finite Element based method developed by Pinho et al. [14,15] consists in the generation of a set of shell Finite Element models of the CT specimen with variable crack lengths that are used to calculate the corresponding values of the J -integral for a unit load. Equipped with this information, it is possible to correlate the experimental results, load and crack length, to the J -integral calculated using Finite Elements, and to generate the corresponding R-curve. However, Finite Element based methods have the additional difficulty of requiring a numerical model and an optically measured crack length.

For the case of the CC tests, there are additional difficulties: the tractions that are transferred along a kink-band render the numerical calculation of the J -integral using the Finite Element Method (FEM) inaccurate. In addition, the experimental determination of the exact location of the tip of a kink-band is even more difficult than for the CT specimens.

Therefore, the objective of this paper is to address these problems by using an alternative method to measure the R-curves based on the Digital Image Correlation (DIC) technique. An automatic algorithm that post-processes the full-field data provided by the DIC system during the CT and CC tests is used to detect the crack tip location and to establish the R-curve from the surface measurements of the displacement and strain fields.

2. Identification of the crack tip location

The algorithm used to identify the crack tip location in the CT and CC test specimens is based on the work of Grégoire [19]. Considering Fig. 1, M and N are two points in the reference image, $\mathbf{d}(\mathbf{x})$ is the displacement of the images, and M^* and N^* are the two points in the deformed image that are separated by a geometric or material discontinuity.

An auxiliary function that identifies a discontinuity in the displacement field, $M \wr N$, is defined as:

$$M \wr N = \left\| \vec{M^*N^*} - \vec{MN} \right\| \quad (1)$$

Eq. (1) can be re-written in terms of the displacements as:

$$M \wr N = \left\| \mathbf{d}(N) - \mathbf{d}(M) \right\| \quad (2)$$

Using (1), the presence of a discontinuity in a pattern $ABCD$ (Fig. 2) is identified in a facet P with the help of the following function:

$$K(P) = \max(A \wr C; B \wr D) \max(\|\mathbf{d}(C) - \mathbf{d}(A)\|; \|\mathbf{d}(D) - \mathbf{d}(B)\|) \quad (3)$$

Eq. (3) quantifies the displacement discontinuity inside the pattern, and Fig. 2 shows that this equation is able to detect a displacement jump associated with a crack, independently of the orientation of the crack within the pattern. To identify whether a pattern is damaged or undamaged a threshold value is associated to this function. It is assumed that the threshold applied is proportional to the mean value of the function $K(P)$ along the facet; therefore, the threshold function $K_T(P)$ is:

$$K(P) \geq \alpha \bar{K} \Rightarrow K_T(P) = 1 \quad (4a)$$

$$K(P) < \alpha \bar{K} \Rightarrow K_T(P) = 0 \quad (4b)$$

$$K(P) = \text{NaN} \Rightarrow K_T(P) = -1 \quad (4c)$$

where \bar{K} is the mean value of $K(P)$ inside the image, α is the threshold value, and NaN indicates that the information it is not available (not a number). Fig. 3 shows a typical relation between the measured crack length of a CT specimen and the time for several values of the parameter α . A small value of α , $\alpha = 2$, was chosen to prevent losing information in vicinity of the crack tip.

Thus, the function $K_T(P)$ represents a mask over the region of interest indexing the following regions:

- $K_T(P) = 1$ are the region where a discontinuity is present but the material is not completely damaged. This happens at the crack tip;
- $K_T(P) = 0$ corresponds to the region where the material is undamaged;

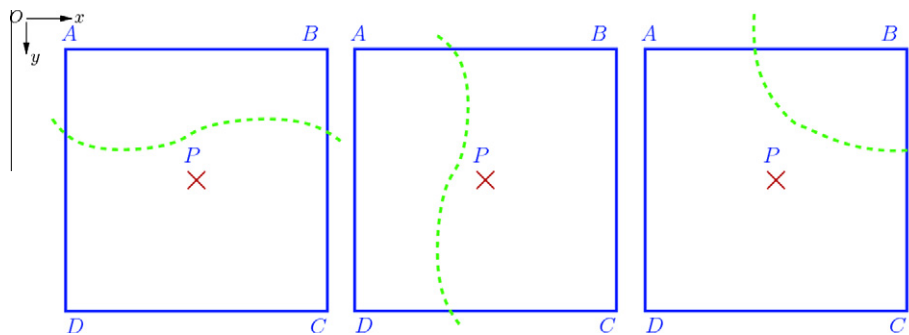


Fig. 2. Different position of the discontinuity with respect to a given pattern.

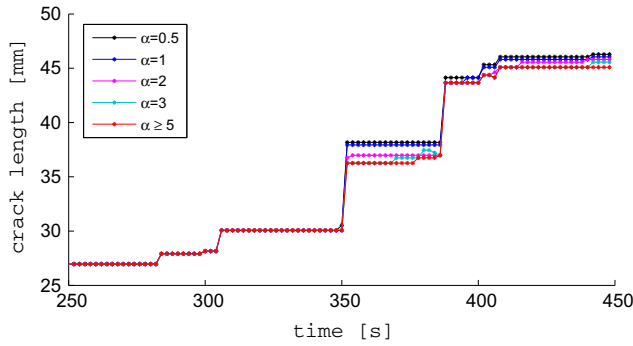


Fig. 3. Relation between the crack length and time for different values of α .

- $K_T(P) = -1$ represents the region where the material is completely damaged and no information is available using digital image correlation.

Fig. 4 shows the K_T function computed for a CT carbon specimen. It can be observed that the function takes the value $K_T = 0$ for the undamaged material points, $K_T = -1$ in the regions where the material is completely fractured, and $K_T = 1$ at the crack tip. The spatial resolution of the K_T function is defined by the size of the subsets used in the DIC method.

3. Experimental determination of the J -integral

Having defined an automatic way to quantify the crack length that does not require any visual inspection, we propose a new method to evaluate the J -integral and to measure the crack resistance curve based on the surface displacement and strain fields obtained from the DIC technique.

For a surface S_0 that surrounds the crack and that includes the edges of the cohesive zone that bridges the crack, the conservation integral, I , can be defined as:

$$I = \frac{1}{h} \int_{S_0} \left(wn_1 - \frac{\partial \mathbf{u}}{\partial x_1} \cdot \mathbf{t} \right) dS = 0 \quad (5)$$

where h is the total thickness of the laminate, w the strain energy density, \mathbf{u} the displacement field and \mathbf{t} the traction vector x_1 is an axis aligned with the crack growth direction and n_1 is the Cartesian coordinate of the unit vector normal to the contour in the x_1 axis.

Taking the contour represented in Fig. 5, defined by $\Gamma \cup C_+ \cup C_0 \cup C_-$, and taking into account that $n_1 = 0$ and $\mathbf{t}^- = -\mathbf{t}^+$ on C_- and C_+ , Eq. (5) results in:

$$\begin{aligned} \frac{1}{h} \int_0^h \left[\int_{\Gamma} \left(wn_1 - \frac{\partial \mathbf{u}}{\partial x_1} \cdot \mathbf{t} \right) dS + \int_0^{\Delta T} \mathbf{t} \cdot d\Delta \right] dx_3 \\ = \frac{1}{h} \int_0^h \left[\int_{\Gamma_0} \left(wn_1 - \frac{\partial \mathbf{u}}{\partial x_1} \cdot \mathbf{t} \right) dS \right] dx_3 \end{aligned} \quad (6)$$

where ΔT is the displacement jump at the beginning of the cohesive zone.

The two terms on the LHS of the previous equation are used to account for the energy-dissipating mechanisms acting on the cohesive zone:

$$J_{\text{coh}} = \frac{1}{h} \int_0^h \int_0^{\Delta T} \mathbf{t} \cdot d\Delta dx_3 \quad (7)$$

and for the energy-dissipating mechanisms acting on the crack tip:

$$J_{\text{tip}} = \frac{1}{h} \int_0^h \left[\int_{\Gamma} \left(wn_1 - \frac{\partial \mathbf{u}}{\partial x_1} \cdot \mathbf{t} \right) dS \right] dx_3 \quad (8)$$

It is clear from Eq. (6) that the contribution of the mechanisms acting at the crack tip and along the cohesive region for the total energy dissipation can be computed from a contour integral that encompasses a region away from the crack tip, i.e. $J_{\text{tip}} + J_{\text{coh}} = J$, with:

$$J = \frac{1}{h} \int_0^h \left[\int_{\Gamma_0} \left(wn_1 - \frac{\partial \mathbf{u}}{\partial x_1} \cdot \mathbf{t} \right) dS \right] dx_3 \quad (9)$$

The contour integral J , which is defined along a region where the material is linear-elastic, is therefore used to calculate the crack resistance curve of the CC and CT test specimens. The CT and CC specimens are manufactured using a cross-ply configuration, $[90/0]_{\text{ns}}$. For these specimens, the J -integral reads:

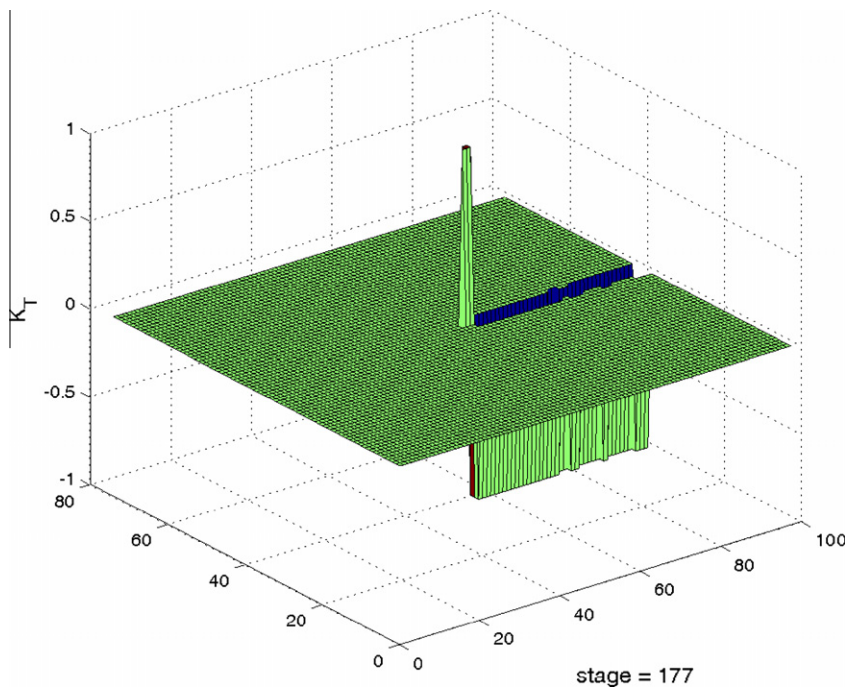


Fig. 4. K_T function.

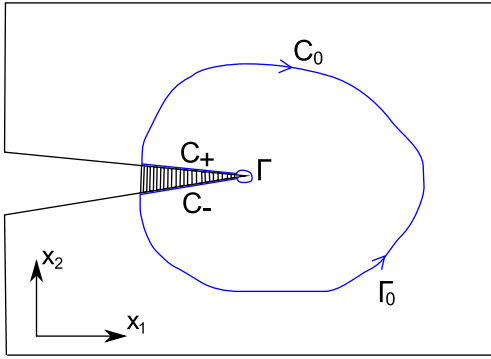


Fig. 5. Conservation integral.

$$J = \frac{1}{h} \int_{\Gamma_0} \left[\sum_{n_0} \int_0^{h^0} \left(w^0 n_1 - \frac{\partial \mathbf{u}}{\partial x_1} \cdot \mathbf{t}^0 \right) dS \right. \\ \left. + \sum_{n_{90}} \int_0^{h^{90}} \left(w^{90} n_1 - \frac{\partial \mathbf{u}}{\partial x_1} \cdot \mathbf{t}^{90} \right) dS \right] dx_3 \quad (10)$$

where n_0 , n_{90} are the number of 0° and 90° plies, respectively, and h^0 , h^{90} are the thickness of each 0° and 90° ply, respectively. w^0 , w^{90} are the strain energy densities in the 0° and 90° plies, respectively.

In the laminates used in this work, the sum of the thicknesses of the all the 0° is equal to half of the laminate thickness. The same happens with the sum of the thicknesses of the all the 90° plies. Taking these facts into account, and assuming linear elasticity along the contour Γ_0 shown in Fig. 5 and that the strain tensor is constant through the thickness of the CT and CC test specimens, the previous equation yields:

$$J = \frac{1}{2} \int_{\Gamma_0} \left[\frac{1}{2} (\boldsymbol{\sigma}^0 + \boldsymbol{\sigma}^{90}) n_1 : \boldsymbol{\varepsilon} - (\boldsymbol{\sigma}^0 + \boldsymbol{\sigma}^{90}) \cdot \mathbf{n} \cdot \frac{\partial \mathbf{u}}{\partial x_1} \right] dS \quad (11)$$

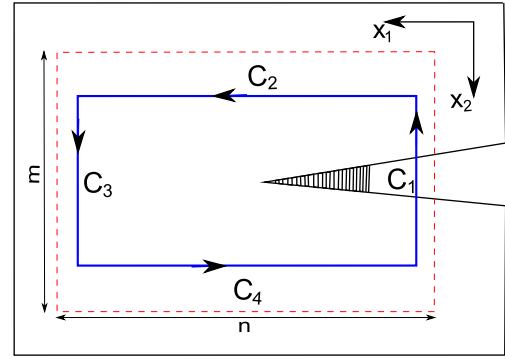
where $\boldsymbol{\sigma}^0$ and $\boldsymbol{\sigma}^{90}$ are respectively the stress fields in the 0° and 90° plies. Defining the laminate average stress as $\bar{\boldsymbol{\sigma}} = \frac{1}{2} (\boldsymbol{\sigma}^0 + \boldsymbol{\sigma}^{90})$, Eq. (11) is written in matrix notation as:

$$J = \frac{1}{2} \int_{\Gamma_0} \left(\{\bar{\boldsymbol{\sigma}}\} \{\boldsymbol{\varepsilon}\}^T n_1 - 2 \left\{ \frac{\partial \mathbf{u}}{\partial x_1} \right\}^T [\bar{\boldsymbol{\sigma}}] \{n\} \right) dS \quad (12)$$

The method proposed in this work consists in determining each term of the previous equation using the displacement and strain fields provided by the DIC system, which are collected in the vectors $\{\mathbf{u}\}$ and $\{\boldsymbol{\varepsilon}\}$, respectively. The first step consists in defining a contour. To simplify the calculations, the simple rectangular contour shown in Fig. 6 is selected.

The calculation of the terms used in (12) is performed as follows:

- Average stresses, $\{\bar{\boldsymbol{\sigma}}\}$. The average stresses are computed from the transformed stiffness matrices of the 0° and 90° plies, $[\bar{\mathbf{C}}^0]$ and $[\bar{\mathbf{C}}^{90}]$ respectively, as $\{\bar{\boldsymbol{\sigma}}\} = \frac{1}{2} ([\bar{\mathbf{C}}^0] + [\bar{\mathbf{C}}^{90}]) \{\boldsymbol{\varepsilon}\}$.
- Differentials dx_1 , dx_2 and dS . The differentials dx_1 and dx_2 are taken as the differences between the centers of adjoining subsets, measured along the corresponding axes. The differential dS is the Euclidian norm of dx_1 and dx_2 .
- Vectors normal to the contour, $\{n\}$. These vectors are directly defined by the simple contour sub-divisions shown in Fig. 6, taking the following forms: $\{1, 0, 0\}^T$ on C_3 , $\{0, 1, 0\}^T$ on C_4 , $\{-1, 0, 0\}^T$ on C_1 , and $\{0, -1, 0\}^T$ on C_2 .
- Derivative of the displacement field, $\left\{ \frac{\partial \mathbf{u}}{\partial x_1} \right\}$. This vector is calculated using the central difference method applied in three adjoining subsets:

Fig. 6. Contour used for the calculation of the J -integral.

$$\left\{ \frac{\partial \mathbf{u}}{\partial x_1} \right\} \approx \left\{ \frac{\Delta \mathbf{u}}{\Delta x_1} \right\} = \left\{ \frac{u^{i+1} - u^{i-1}}{2 \Delta x_1} \right\} \quad (13)$$

Having calculated all the terms required in Eq. (12), the J -integral is computed from the summation of all discrete contributions of each subset, which are calculated as previously explained.

This method was implemented in a "Matlab" [20] script that generate an R-curve automatically by assigning to each measured crack length its corresponding value of the J -integral.

4. Experimental tests

4.1. Configuration of the test specimens

The material used in this work is unidirectional carbon-fiber reinforced epoxy Hexcel IM7-8552. The elastic properties of IM7-8552, measured in a previous investigation [18], are shown in Table 1.

E_1 and E_2 are the longitudinal and transverse Young's modulus respectively, G_{12} is the shear modulus, and ν_{12} is the major Poisson's ratio.

The pre-impregnated plies were laid-up in an $[90/0]_{8s}$ configuration proposed in [14] and cured according to Hexcel's specifications. The resulting plates were cut using a diamond-coated disk to their nominal overall dimensions, which are based on the work of Pinho et al. [14]. The specimens were finally machined to their final geometry, shown in Fig. 7 (CT specimen), and in Fig. 8 (CC specimen). The holes for the load introduction pins shown in Figs. 7 and 8 were cut using tungsten carbide drills while clamping the specimens between two sacrificial carbon-epoxy plates. This procedure prevents delamination at the entrance and exit of the drill.

The CT and CC tests were conducted using a servo-hydraulic MTS 312.31 test machine with a load capacity of 250 kN. The tests were performed using a 100 kN load cell and at controlled speed of 2 mm/min. Fig. 9 shows the set-up used during one CT tests. The test specimen was previously sprayed with a white and black ink to generate a random and contrasted distribution of granular spots, as required by the DIC system. The average size of the granular spots was suitable with regard to the resolution necessary for the measurement of the energy release rate.

Table 1
IM7-8552 ply elastic properties.

Property	Mean value
E_1 (GPa)	171.42
E_2 (GPa)	9.08
G_{12} (GPa)	5.29
ν_{12}	0.32

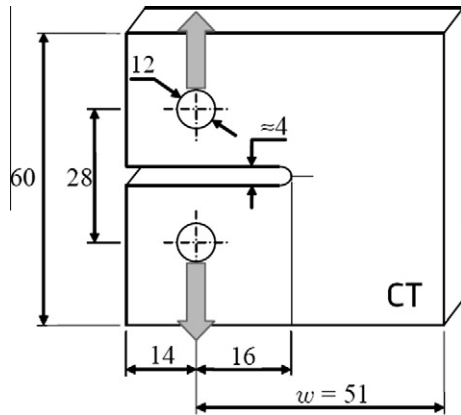


Fig. 7. Geometry of compact tension test specimen (after [14], dimensions in mm).

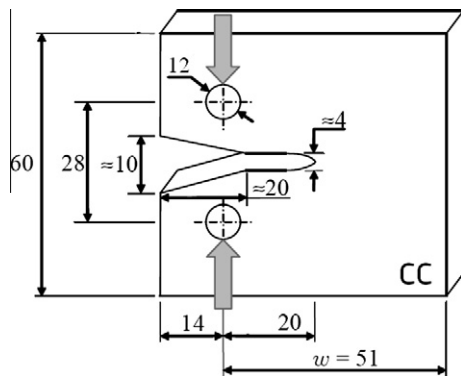


Fig. 8. Geometry of compact compression test specimen (after [14], dimensions in mm).

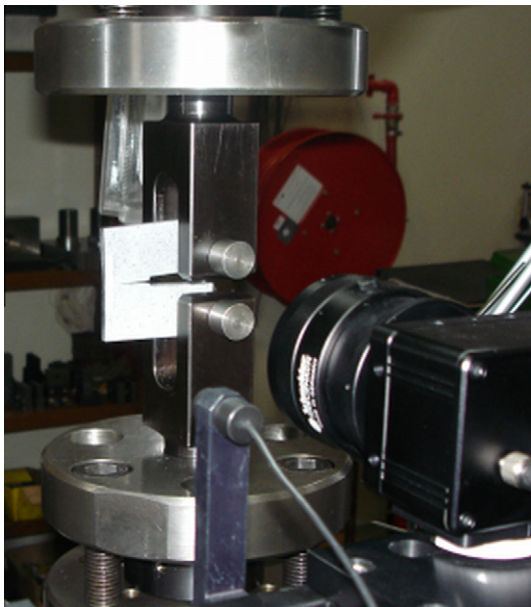


Fig. 9. Compact tension test specimen and DIC system.

The single-camera ARAMIS digital image correlation software developed by GOM [21] was used. This measurement system is equipped with an 8-bit Baumer Optronic FWX20 camera (resolution of 1624×1236 pixels, pixel size of $4.4 \mu\text{m}$ and sensor format of $1/1.8''$) coupled with a Schneider-Kreuznach Componar-S

50 mm $f/2.8$ lens. For mobility and adaptability, the camera was mounted on a tripod, which was positioned facing the testing machine. In the set-up, the optical system was positioned perpendicular to the surface of the specimen mounted into the testing machine (Fig. 9).

A laser pointer was used to facilitate a correct alignment. The working distance (defined between the specimen's surface and the support of the cameras) was set in the range of 0.8 m. The lens was adjusted to be in focus with regard to the surface of interest, setting the lens aperture to $f/2.8$ in order to minimize the depth of field. The aperture of the lens was then closed ($f/11$) to improve the depth of field during testing. The shutter time was set to $1/20$ s, a value appropriate for the cross-head displacement rate used during testing (2 mm/min), and the size of the camera unit cells ($4.4 \mu\text{m}$). The light source was finally adjusted in order to guarantee an even illumination of the specimen's surface and to avoid over-exposition (i.e., the saturation of pixels over the field of view).

The region of interest was set to approximately $20 \times 20 \text{ mm}^2$, which defines a conversion factor of about $0.185 \text{ mm pixel}^{-1}$. In the digital image correlation method, the displacement field is measured by analyzing the geometrical deformation of the images of the surface of interest, recorded before and after loading. For this purpose, the initial (undeformed) image was mapped by square facets (subsets), within which an independent measurement of the displacement is calculated. Therefore, the facet size, on the plane of the object, will characterize the displacement spatial resolution. The facet step (i.e., the distance between adjacent facets) can also be set either for controlling the total number of measuring points over the region of interest, or for enhancing the spatial resolution by slightly overlapping adjacent facets. Typically, a larger facet size will improve the precision of the measurements but also will degrade the spatial resolution [22]. Thus, a compromise must be found according to the application to be handled. In this work, a facet size of 15×15 pixels was chosen, attending to the size of the region of interest, the optical system (magnification) and the quality of the granulate (average speckle size) obtained by the spray paint. The facet step was also set to 15×15 pixels to avoid statistically correlated measurements. The in-plane displacements were then numerically differentiated in order to determine the strain field need for the calculation of the J -integral using the procedure previously presented.

A typical strain field obtained by ARAMIS [21] for the CT test specimens is shown in Fig. 10.

4.2. Compact tension

A typical load–displacement relation obtained in the CT tests is shown in Fig. 11. The load was measured using the 100 kN load cell, and the displacement was measured using the linear variable differential transformer (LVDT) connected to the hydraulic actuator of the test machine. Three CT specimens were tested.

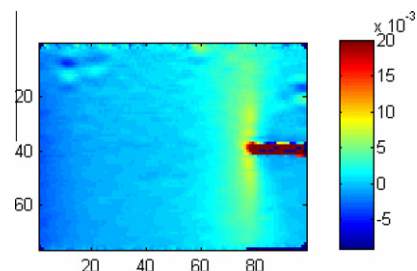


Fig. 10. Strain field obtained by ARAMIS: $\epsilon_{yy}(x)$, with 0-y perpendicular to the crack.

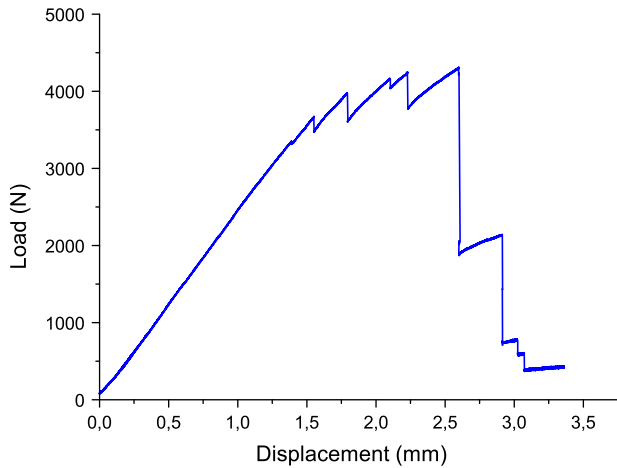


Fig. 11. Load–displacement in a CT test specimen.

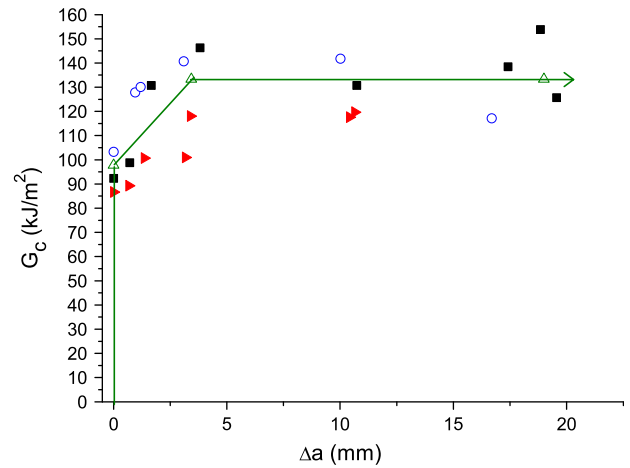


Fig. 13. R-curves extracted from all CT specimens using DIC, and corresponding mean R-curve. Each symbol corresponds to one CT test.

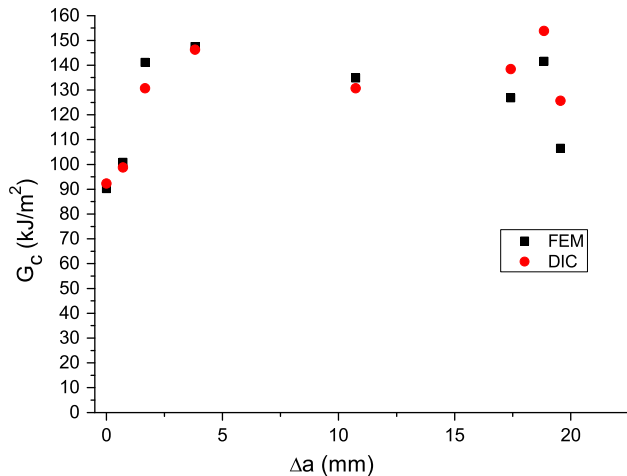


Fig. 12. R-curves extracted from a CT specimen using FEM and DIC.

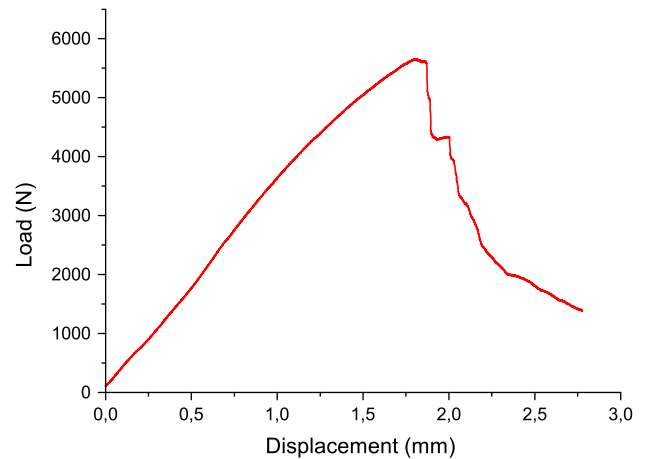


Fig. 14. Load–displacement in a CC test specimen.

Fig. 11 shows that the load–displacement relation is linear up to approximately 80% of the peak load, and that crack propagation occurs in discrete jumps.

Fig. 12 shows the R-curve measured from the FEM post-processing of the test results method proposed by Pinho et al. [14] and that obtained by post-processing the displacement and strain fields measured by the DIC system.

Fig. 12 shows a good correlation between the FEM and DIC data reduction methods. This means that the fracture process zone that bridges the crack has a minor effect on the displacement and strain fields in the regions where the Finite Element model computes the J -integral.

Fig. 13 shows the R-curves obtained from the three CT tests. Fig. 13 also shows the mean value of the fracture process zone, 3.4 mm, and the mean values of the initial fracture toughness and that corresponding to steady-state crack propagation, 97.8 kJ/m² and 133.3 kJ/m² respectively. These values are slightly lower than the mean values of the fracture toughness for initiation and steady-state propagation, 113.8 kJ/m² and 146.7 kJ/m² respectively, measured by Pinho [23] for the same material system.

4.3. Compact compression

A typical load–displacement relation obtained from a CC test is shown in Fig. 14.

A non-linear response is observed in the load–displacement relation before the peak load is attained. This non-linearity of the curve is likely to be caused by the plastic deformation of the resin at the load introduction points. In fact, the cross-ply laminate used triggers high in-plane shear stresses that lead to plastic deformation of the resin at the load introduction points. This effect was explained in detail by Chang in his analysis of bolted joints [24]. The plasticity at the load introduction points does not affect the measured R-curve because the contour selected does not include the vicinity of the load introduction points.

Fig. 15 shows the R-curve measured from the FEM post-processing of the test results obtained by the method proposed by Pinho et al. [14] and the R-curve obtained using the DIC data reduction procedure proposed here.

Fig. 15 shows that the FEM-based solution yields unrealistically high values of the fracture toughness during the propagation of fiber kink-bands. This result is in agreement with the findings of Pinho et al. [14]. For 15 mm of kink-band propagation the fracture toughness computed using the FEM is approximately twice that calculated using the DIC system. The reason for this fact is that the FEM-based calculation of the J -integral does not account for the contact and load transfer across the band of the kinked fibers. These effects clearly affect the displacement and strain fields along the contours of the J -integral computed using FEM. On the other hand, the DIC-based method uses the actual displacement and

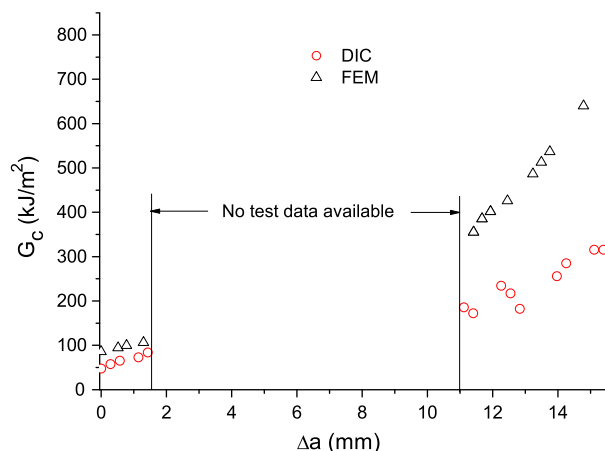


Fig. 15. R-curves extracted from a CC specimen using FEM and DIC.

strain fields on the surface of the specimen, provided that the contours selected do not include delaminated regions, thus resulting in an improved R-curve. However, the contact stresses that are transferred along the kink-band still pollute the data obtained using DIC because they introduce one additional term on the LHS of Eq. (6).

Delamination associated with the propagation of the kink-band from the initial notch was also observed in the CC tests. The presence of delamination renders this test method unsuitable to measure the R-curve in compression because there is another energy-dissipating mechanism apart from those related to the kink-band itself. In addition, the presence of delamination invalidates the assumption of a two-dimensional crack, and of constant strain through the thickness of the laminate (assumption used in Eq. (6)). Delamination was also the reason why the DIC-based method could not detect the tip of the kink-band for $2 \text{ mm} \leq \Delta a \leq 11 \text{ mm}$. The out-of-plane displacement of the delaminated plies renders the experimental determination of the displacement and strain fields impossible with just one camera. The delamination propagation stopped after 11 mm of kink-band propagation, and the identification of its extremity was again possible.

5. Conclusions

This paper presents a new method to measure the crack resistance curves in CT and CC test specimens manufactured using cross-ply CFRP composite laminates. The method is based on the measurement of the displacement and strain fields using DIC. These fields are the basis for the rigorous determination of the location of the surface crack or of the kink-band tip (in the absence of delamination), and for the automatic computation of the J -integral. The method was implemented in a "Matlab" code that obviates the need of any complex pre- and post-processing of the test data, either based on FEM or standard data reduction methods, and enables the real-time generation of R-curves during a test.

The comparison between the R-curves obtained in CT specimens using the FE-based post-processing and the DIC-based method indicates that the results are virtually the same and that the method proposed here is a valid alternative to measure R-curves associated with longitudinal tensile failure mechanisms in composite materials. The initiation value of the fracture toughness associated with longitudinal tensile failure mechanisms in IM7-8552 is 98.7 kJ/m^2 , and it raised up to 133.7 kJ/m^2 for steady-state propagation. The mean value of the associated cohesive zone is 3.4 mm .

It is concluded that the FE-based data reduction method is inadequate for the measurement of R-curves in CC specimens because

it severely overpredicts the fracture toughness. This is in agreement with the findings of Pinho et al. [14]. The DIC-based method is an improvement over FE-based data reduction methods because it is based on the actual displacement field on a pre-defined contour that does not include delaminated regions. However, the contribution of the contact tractions to the J -integral still needs to be quantified and used in the data reduction method to improve the accuracy of the data. The initial value of the fracture toughness associated with longitudinal compressive failure mechanisms in IM7-8552 measured using DIC was 47.5 kJ/m^2 ; the measured fracture toughness increased up to 315 kJ/m^2 for 15 mm of propagation of a kink-band. However, the values computed for the fracture toughness using the CC specimen do not account for the energy dissipated by the delamination that accompanied the propagation of the kink-band. In addition, the delamination does not allow the accurate measurement of the tip of the kink-band. Therefore, it is concluded that these difficulties render the CC test method unsuitable to generate R-curves and that an alternative test method should be developed.

Acknowledgements

The first author acknowledges the financial support of the European Commission under Contract No. MRTN-CT-2005-019198. The financial support of the Portuguese Foundation for Science and Technology (FCT) under the Project PDCTE-EME-65099-2003 is acknowledged by the second author.

References

- [1] Dávila CG, Camanho PP, Rose CA. Failure criteria for FRP laminates. *J Compos Mater* 2005;39:323–45.
- [2] Camanho PP, Dávila CG, Pinho ST, Iannucci L, Robinson P. Prediction of in-situ strengths and matrix cracking in composites under transverse tension and in-plane shear. *Composites – Part A* 2006;37:165–76.
- [3] Puck A, Schürmann H. Failure analysis of FRP laminates by means of physically based phenomenological models. *Compos Sci Technol* 1998;58:1045–67.
- [4] Kuraishi A, Tsai SW, Liu KKS. A progressive quadratic failure criterion – part B. *Compos Sci Technol* 2002;62:1683–95.
- [5] Maimí P, Camanho PP, Mayugo JA, Dávila CG. A continuum damage model for composite laminates: part I – constitutive model. *Mech Mater* 2007;39:897–908.
- [6] Maimí P, Camanho PP, Mayugo JA, Dávila CG. A continuum damage model for composite laminates: part II – computational implementation and validation. *Mech Mater* 2006;39:909–19.
- [7] Lapczyk I, Hurtado J. Progressive damage modeling in fiber-reinforced materials. *Composites – Part A* 2007;38:2333–41.
- [8] Van Der Meer FP, Sluys LJ. Continuum models for the analysis of progressive failure in composite laminates. *J Compos Mater* 2009;43:2131–56.
- [9] Larve EV, Mollenhauer DH, Zhou EG, Breitzman T, Whitney TJ. Independent mesh method-based prediction of local and volume average fields in textile composites. *Composites – Part A* 2009;40:1880–90.
- [10] Turon A, Camanho PP, Costa J, Dávila CG. A damage model for the simulation of delamination in advanced composites under variable-mode loading. *Mech Mater* 2006;38:1072–89.
- [11] Jiang W-G, Hallett SR, Green BG, Wisnom MR. A concise interface constitutive law for analysis of delamination and splitting in composite materials and its application to scaled notched tensile specimens. *Int J Numer Methods Eng* 2007;69:1982–95.
- [12] Sørensen BF, Jacobsen TK. Large-scale bridging in composites: R-curves and bridging laws. *Composites – Part A* 1998;29:1443–51.
- [13] Dávila CG, Rose CA, Camanho PP. R-curve toughening in the longitudinal fracture of composites and associated cohesive law. *Int J Fract* 2009;158:211–23.
- [14] Pinho ST, Robinson P, Iannucci L. Fracture toughness of the tensile and compressive fibre failure modes in laminated composites. *Compos Sci Technol* 2006;66:2069–79.
- [15] Laffan MJ, Pinho ST, Robinson P, Iannucci L. Measurement of the in situ ply fracture toughness associated with mode I fibre tensile failure in FRP. Part I: data reduction. *Compos Sci Technol* 2010;70:606–13.
- [16] Rice JR. A path independent integral and the approximate analysis of strain concentration by notches and cracks. *J Appl Mech* 1968;31:379–86.
- [17] ASTM E399-06. Standard test method for linear-elastic plane-strain fracture toughness of metallic materials; 2006.

- [18] Camanho PP, Maimí P, Dávila CG. Prediction of size effects in notched laminates using continuum damage mechanics. *Compos Sci Technol* 2007;67:2715–27.
- [19] Grégoire D. Initiation, propagation, arrêt et redémarrage de fissures sous impact. PhD Thesis, LaMCoS-INSA de Lyon; 2008.
- [20] The MathWorks, Inc., 3 Apple Hill Drive Natick, MA 01760-2098, USA.
- [21] GOM International AG, Bremgarterstrasse 89B, CH-8967 Widen, Switzerland.
- [22] Lecompte D, Smits A, Bossuyt S, Sol H, Vantomme J, Van Hemelrijck D, et al. Quality assessment of speckle patterns for digital image correlation. *Opt Lasers Eng* 2006;44:1132–45.
- [23] Pinho ST. Private communication; 2009.
- [24] Chang FK, Scott RA, Springer GS. Failure strength of nonlinearly elastic composite laminates containing a pin loaded hole. *J Compos Mater* 1984;18:464–77.